RESEARCH ARTICLE

An Adaptable Physiological Model of Endocytic Megalin Trafficking in Opossum Kidney Cells and Mouse Kidney Proximal Tubule

Katherine E. Shipman, Kimberly R. Long, Isabella A. Cowan, Youssef Rbaibi, Catherine J. Baty, Ora A. Weisz*

Renal Electrolyte Division, Department of Medicine, University of Pittsburgh School of Medicine, Pittsburgh, PA 15213, USA
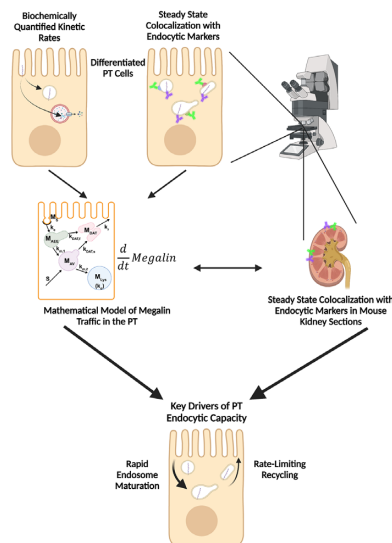
*Address correspondence to O.A.W. (e-mail: weisz@pitt.edu)

Abstract

The cells that comprise the proximal tubule (PT) are specialized for high-capacity apical endocytosis necessary to maintain a protein-free urine. Filtered proteins are reclaimed via receptor-mediated endocytosis facilitated by the multiligand receptors megalin and cubilin. Despite the importance of this pathway, we lack a detailed understanding of megalin trafficking kinetics and how they are regulated. Here, we utilized biochemical and quantitative imaging methods in a highly differentiated model of opossum kidney (OK) cells and in mouse kidney in vivo to develop mathematical models of megalin traffic. A preliminary model based on biochemically quantified kinetic parameters was refined by colocalization of megalin with individual apical endocytic compartment markers. Our model predicts that megalin is rapidly internalized, resulting in primarily intracellular distribution of the receptor at steady state. Moreover, our data show that early endosomes mature rapidly in PT cells and suggest that Rab11 is the primary mediator of apical recycling of megalin from maturing endocytic compartments. Apical recycling represents the rate-limiting component of endocytic traffic, suggesting that this step has the largest impact in determining the endocytic capacity of PT cells. Adaptation of our model to the S1 segment of mouse PT using colocalization data obtained in kidney sections confirms basic aspects of our model and suggests that our OK cell model largely recapitulates in vivo membrane trafficking kinetics. We provide a downloadable application that can be used to adapt our working parameters to further study how endocytic capacity of PT cells may be altered under normal and disease conditions.

Key words: kidney; endocytosis; megalin; kinetics

Introduction

The polarized epithelial cells that comprise the proximal tubule (PT) are specialized to carry out the high-capacity apical endocytosis necessary to recover essential nutrients and maintain a protein-free urine. Mutations in essential components of the endocytic pathway or impairments in its regulation lead to proteinuric disease and are associated with progression of kidney injury.[1,2] Despite its critical relevance to PT function, our understanding of how this pathway operates to maintain the efficient recovery of filtered proteins remains limited. These gaps in our knowledge reflect both the complexity of the endocytic pathway itself and the technical challenges of studying PT function in vivo.

The PT is divided into 3 subsegments, denoted S1, S2, and S3. The multiligand receptors megalin and cubilin expressed in these cells facilitate the uptake of albumin and other serum proteins that escape the glomerular filtration barrier. The majority of normally filtered ligands are recovered in the S1 segment, whereas later segments provide additional capacity for retrieval of excess filtered proteins under nephrotic conditions.[3–6] Megalin is a ~600 kDa transmembrane member of the low-density lipoprotein receptor family, whereas cubilin (~460 kDa) lacks a transmembrane domain and cytoplasmic tail and assembles as a trimer with the membrane-associated amnionless (~50 kDa) for targeting to the apical membrane as a cubilin-amnionless (CUBAM) complex.[1,2,7,8] Megalin and CUBAM each contain Dab2-interacting endocytic motifs and can function as independent receptors, but biochemical and morphological studies demonstrate that the receptors form a complex and traffic together in the PT.[9,10] Loss of function of either receptor results in the urinary excretion of normally filtered ligands, termed tubular, or low molecular weight proteinuria.[11,12]

Ultrastructural studies of the rodent PT in vivo have illuminated the morphological characteristics of the apical endocytic pathway and its marked differences from that in other cell types. The apical surface of PT cells is comprised of an extensive brush border, with numerous irregularly sized clathrin-coated pits observed at the base of the microvilli.[13–15] Endocytosed ligands are internalized into vesicles originating from these invaginations. The vesicles fuse with small apical endocytic endosomes (AEEs) that mature into larger apical vacuoles (AVs). Maturation is associated with increased acidification of these endocytic compartments, which promotes dissociation of ligands from megalin and CUBAM receptors. Content from these fluid-rich vacuoles is delivered to lysosomes, where ligands are degraded,[15,16] while receptors are believed to recycle to the apical membrane via a large network of dense apical tubules (DATs) that emanate from both AEEs and AVs.[15–17] In the current model, based on data from other cell types, recycling has been categorized as "fast recycling" that initiates from early sorting endosomes and "slow recycling" that occurs from later recycling endosomes. Rab4 has been shown to play a role in fast recycling, whereas Rab11 is essential for slow recycling.[18] Whether fast and slow recycling occurs in PT cells, in which compartments these steps originate, and whether these processes are differentially regulated by Rab proteins remains unknown.

There have been previous attempts to mathematically describe the uniquely robust endocytic and recycling pathways of the PT. Nielsen and colleagues developed an elegant model of membrane traffic in the PT based on ultrastructural analysis and morphometry of rat kidney sections, which provided key insights into the structure of endocytic and recycling compartments.[19] Combining their data with previous studies examining temporal PT membrane labeling with cationized ferritin,[20] the authors estimated rates for membrane flux through the apical pathway. Their model reasonably postulates that endocytosis occurs very rapidly, that most internalized membrane is rapidly transported to DATs for recycling, and that only a small fraction of membrane is transferred to lysosomes. However, this study could not assess megalin trafficking kinetics or its distribution among the endocytic compartments. More recently, Perez Bay et al. (2016) developed a kinetic model to describe the trafficking of heterologously expressed tagged truncated megalin construct in Madin–Darby canine kidney (MDCK) cells, which do not express endogenous megalin. This study concluded that apically

internalized receptor is transported to common recycling endosomes where it intersects the trafficking pathways for basolaterally internalized and transcytosing proteins before being recycled back to the apical surface.[21] A significant limitation of this model is that the apical endocytic pathway in MDCK cells is organized very differently from that described in PT cells, and is far less robust than that of PT cells in vivo.[22–24]

The unique organization and very rapid membrane flux through the endocytic pathway in PT cells highlight the need for a cell-type-specific understanding of how the pathway is regulated. We have previously demonstrated that opossum kidney (OK) cells cultured under continuous orbital shear stress represent a well-differentiated cell culture model that better replicates essential features of PT structure and function compared with cells cultured under static conditions.[25] Our optimized model maintains high apical endocytic capacity, increased expression of megalin, cubilin, and Dab2, robust ion transport activity, and, comparable to the PT in vivo, a metabolism that relies on oxidative phosphorylation rather than glycolysis.[25,26] The organization and ultrastructural morphology of endocytic compartments in cells grown in this manner closely resemble those described in vivo.[25] The transcriptional profile of these cells most closely resembles that of the S1 segments of the PT.[27–30] Indeed, in stark contrast to the much weaker megalin expression in other cell culture models of PT cells, the *Lrp2* mRNA that encodes megalin is the most abundant transcript in OK cells cultured under these conditions.[31,32]

Here, we combined biochemical and quantitative imaging techniques to develop new models that describe megalin traffic and distribution among endocytic compartments in shear-stress differentiated OK cells and in the mouse S1 segment in vivo. We identified specific markers for individual endocytic compartments and refined the current organizational model of the PT apical endocytic pathway. Our model highlights the critical features of this pathway needed to maintain the high endocytic capacity of these cells. We find that maturation of AEEs to AVs occurs very rapidly in PT cells and that most recycling occurs from the latter compartment. Moreover, our model shows that the rates dictating megalin recycling play the largest role in determining overall endocytic capacity of PT cells. The kinetics of membrane traffic in fully differentiated OK cells are comparable to those in S1 cells in vivo, further validating the utility of this cell culture system as a model to study PT function. Finally, we provide a downloadable application encoding our model that can be used to make predictions of how megalin traffic in PT cells is modulated under normal conditions and in disease.

Materials and Methods

Cell Culture

OK-P cells, originally obtained at low passage from Dr. Moshe Levi (Georgetown University) were cultured in DMEM-F12 (Sigma; D6421), 5% fetal bovine serum (FBS), and $2.5\times$ GlutaMax (Gibco; 35050–061) at 37°C and 5% CO_2. OK cells were seeded onto 12 mm Transwell permeable supports (Costar; 3401) in 12-well dishes at 4×10^5 cells per 0.5 mL medium on the apical side of the filter. The basolateral side of the filter received 1.5 mL of medium. After overnight incubation, the filters were transferred to an orbital platform shaker in the incubator and rotated at 15.3 rad/s (146 rpm) for 72 h to enhance differentiation as described in Long et al.[25] Media was changed daily.

Surface Biotinylation Based Assays

Endocytosis

After washing with cold phosphate-buffered saline containing $MgCl_2$ and $CaCl_2$ (PBS; Sigma, D8662), the apical surface of OK cells cultured on permeable supports under shear stress was biotinylated with 1 mg/mL EZ-Link Sulfo-NHS-SS-biotin (Thermo Scientific, 21331) in 0.5 mL TEA-buffered saline (TBS; 10 mM triethanolamine-HCl, pH 7.6, 137 mM NaCl, 1 mM $CaCl_2$) for 2×15 min on ice. The biotinylation reaction was quenched by washing with DMEM-F12 plus 5% FBS for 10 min on ice. Samples were rinsed once with ice cold DMEM-F12, $2.5\times$ Glutamax, and 25 mM HEPES (Gibco, 15630–080; DF + H media), then quickly warmed to 37°C by the addition of prewarmed DF + H media and placed on an orbital sharker in the incubator (146 rpm) for 0–5 min. Endocytosis was stopped by washing with prechilled PBS on ice. Biotin at the cell surface was stripped by washing cells with prechilled 100 mM MESNA in Stripping Buffer (50 mM Tris-HCl pH 8.6, 100 mM NaCl, 1 mM EDTA, 0.2% BSA) for 2×20 min on ice. A duplicate 0 min time-point was left unstripped to estimate the fraction of total megalin at the apical surface at steady state. Residual MESNA was quenched by washing cells with ice cold DF + H media for 10 min on ice. Filters were washed with ice-cold PBS, excised with a clean razor blade, and solubilized in 0.6 mL detergent lysis buffer (50 mM Tris, pH 8.0, 62.5 mM EDTA, 1% IGEPAL CA-630, 4 mg/mL deoxycholate, 5 μg/mL leupeptin, 7 μg/mL pepstatin A, 1 mM phenylmethylsulfonyl fluoride, and Complete Protease Inhibitor EDTA-Free (Roche, 04693159001; 1 tablet/10 mL of buffer) for 20 min at 37°C. To determine total megalin levels, 5% of the lysate volume was reserved. Biotinylated proteins were precipitated from the remaining lysate by overnight incubation at 4°C with streptavidin agarose resin (Thermo Scientific, #20353) and recovered in $4\times$ loading sample buffer (0.2 M Tris–HCl pH 6.8, 8.6 M glycerol, 8% SDS, 0.025% bromophenol blue) with 5% 2-mercaptoethanol by heating at 98°C for 5 min. Samples were analyzed by western blot after SDS-PAGE on 4–15% Criterion TGX (Bio-Rad, 5671083) gels. Megalin was detected with antimegalin antibody generously provided by Dr. Daniel Biemesderfer and Dr. Peter Aronson (Yale University, MC-220, 1:20,000).[33]

Surface Half-Life

The apical surface of filter-grown OK cells was biotinylated as above. Cells were rinsed once with ice cold DF + H media then quickly warmed to 37°C by the addition of prewarmed DF + H media and placed on a rotating shaker in the incubator. At each time point starting from 1 to 8 h, filters were rinsed in cold PBS, cells were lysed, biotinylated proteins were recovered, and samples were immunoblotted for megalin as described earlier.

Indirect Immunofluorescence in OK Cells

Filters were washed in warm PBS and fixed in warm 4% paraformaldehyde (PFA) and 100 mM sodium cacodylate at ambient temperature. After 2 washes in PBS, the filters were quenched (PBS, 20 mM glycine, and 75 mM ammonium chloride) for 5 min and permeabilized for 7 min in quench solution containing 0.1% Triton X-100. After being washed with PBS, the filters were blocked with PBS, 1% BSA, and 0.1% saponin, and incubated for 1 h with primary antibody diluted in PBS, 0.5% BSA, and 0.025% saponin (wash buffer). The filters were washed 3 times, incubated for 30 min with secondary antibody diluted in wash buffer, and washed 3 times. After excising, filters were mounted

onto glass slides with ProLong Gold Antifade Mountant (Molecular Probes, P36935) or ProLong Glass Antifade Mountant (Invitrogen, P36980), depending on the immersion fluid of the objective, with a No 1.5 cover glass (Fisher Scientific, 12541A). Antibodies, sources, and dilutions used for indirect immunofluorescence in OK cells are listed in Table S1. For labeling with lysosomes, cells were incubated with 100 nM LysoTracker Red DND-99 (Invitrogen, L7528) in DF + H media for 30 min on a rotating shaker in the incubator prior to fixation.

For co-staining with primary antibodies from different host species, filters were incubated with both primary antibodies simultaneously followed by both secondary antibodies. When co-staining with primary antibodies from the same host species (eg, Rab11 and Megalin or EEA1 and Rab7), labeling was done sequentially.[34] Filters were incubated with the first primary antibody for 1 h, followed by a fluorophore conjugated F(ab) fragment for 30 min. Filters were then incubated with unconjugated F(ab) fragment diluted in wash buffer for 30 min to block any remaining unbound sites on the prior to sequential incubation the second primary and secondary antibodies.

Filters were imaged on a Leica TCA SP5 or Stellaris 8 confocal microscope using a 63× glycerol or oil (respectively) immersion objective (NA 1.4). Images were acquired with a voxel size of 45 × 45 × 130 nm (x, y, z). All images were deconvolved with Huygens Essential version 17.04 using the CMLE algorithm, with SNR: 20 and 40 iterations (Scientific Volume Imaging, The Netherlands, http://svi.nl). Colocalization of 2 channels over the whole z-stack was determined by Manders' coefficients using the JACoP plugin for ImageJ without thresholding.[35,36] The Manders' coefficient represents the fraction or percentage of all the positive pixels in 1 channel that overlap with positive pixels from another channel.[37] We occasionally refer to these measurements with the following nomenclature, using EEA1 and Rab7 as an example: the percentage of total EEA1 pixels that overlap with Rab7 pixels is $EEA1_{Rab7}$ and the percentage of total Rab7 pixels that overlap with EEA1 pixels is $Rab7_{EEA1}$. Megalin is typically abbreviated to M when its colocalization is described this way.

The fractional distribution of markers over the z-axis was determined by dividing the sum of pixel intensities in each plane by the total pixel intensity in the whole z-stack for each marker. The z position was normalized by dividing by the total number of z-steps in the stack. The fractional distribution of each marker was averaged across all images after interpolation. The number of replicates indicated in figure legends for these data is the number of fields analyzed from 3 to 5 independent experiments.

Indirect Immunofluorescence in Mouse Kidney Sections

Five mice (1 female 129/Sv mouse, 24 wk old; 2 female and 2 male C57BL/6 mice, 16 wk old) were anesthetized using isoflurane and perfused intracardially with cold PBS. Kidneys were fixed initially by perfusion with cold 4% PFA in cacodylate buffer (pH 7.4) and further, after harvest and bisection, for 2 h in 4% PFA on ice. Tissue was dehydrated in 30% sucrose and embedded in O.C.T. compound (Scigen 4583) at −80°C.

A double/sequential labeling protocol was used to stain kidney sections with primary antibodies from the same host species.[34] Cryostat sections (10 mm) were placed on slides, rehydrated in PBS for 30 min, permeabilized with 0.1% TritonX-100 for 10 min, and blocked with 1% BSA, 5% normal goat serum, and 0.1% saponin for 15 min. Sections were blocked again with 100 µg/mL goat antimouse unconjugated F(ab) fragments in 0.5% BSA and 0.1% saponin for 15 min. Sections were incubated

for 1 h with the first primary antibody (eg, rabbit anti-SGTL2), washed 3 times for 5 min each in wash buffer (1× PBS, 0.5% BSA, and 0.025% saponin), and incubated for 30 min with either antimouse or antirabbit fluorophore conjugated F(ab) fragment secondary, depending on the host species of the first primary antibody. After being washed 3 times in wash buffer, sections were blocked with 100 µg/mL goat antimouse or goat antirabbit unconjugated F(ab) fragments (depending on the host species of the first primary antibody) in 0.5% BSA and 0.1% saponin for 15 min. After rinsing with PBS, sections were incubated for 1 h with the second and third primary antibodies (eg, rabbit anti-Rab11 and mouse anti-Rab7), washed 3 times for 5 min each in wash buffer and incubated for 30 min with corresponding fluorophore conjugated secondary antibodies. After washing 2 times in wash buffer and once in PBS, sections were mounted using with ProLong Gold Antifade Mountant with a No 1.5 cover glass (Thermo Scientific, 3422). Megalin and LAMP1 were also stained sequentially and blocked to prevent cross-species binding of goat antimouse secondary to rat primary. Antibodies used for indirect immunofluorescence in mouse kidney sections are listed in Table S2.

Sections were imaged on Leica SP8 confocal microscope with a 63× oil objective (NA 1.4). Images were acquired with a voxel size of 40 × 40 × 130 nm (x, y, z). Images were deconvolved with Huygens Essential version 17.04 using the CMLE algorithm, with SNR: 20 and 40 iterations. Masks were drawn by hand in ImageJ to only include the region within the end-on tubule of interest and to exclude background binding of antimouse secondary to the outside of tubules (see Figure S6F). The colocalization of 2 channels over the entire z-stack only within the mask region was determined by Manders' coefficients, which were calculated using MATLAB R2021a (The MathWorks Inc., Natick, MA, USA).

Preliminary Model of Megalin Traffic From Biochemical Data

This model describes the trafficking of megalin in a PT cell based on experimental biochemical data, depicted graphically in Figure 1D. At any given time, megalin (M) is divided into 2 pools: the % at the apical surface ($M_S(t)$) and the % intracellular ($M_I(t)$) such that the total amount of megalin is $M_T(t) = M_S(t) + M_I(t) = 100$.

The following system of ordinary differential equations describes the trafficking between these 2 pools of megalin:

$$\frac{dM_S}{dt} = -k_e M_S + k_R M_I, \tag{1a}$$

$$\frac{dM_I}{dt} = k_e M_S - (k_R + k_D) M_I + S, \tag{1b}$$

where k_e is the endocytic rate, k_R is the recycling rate, k_D is the degradation rate, and S is the synthesis rate. At steady state (denoted by ∗), when both equations are set to zero, the distribution of megalin can be defined as

$$M_S^* = \frac{k_R S}{k_e k_D}, \tag{2a}$$

$$M_I^* = \frac{S}{k_D}. \tag{2b}$$

Trafficking of Biotinylated Megalin
To describe the trafficking of biotinylated megalin, the synthesis rate S is set to zero, since no new biotinylated megalin is created following the surface labeling. Initially, all biotinylated megalin is at the apical surface so the system has the initial conditions $M_S(0) = 100$ and $M_I(0) = 0$. With these initial conditions, the
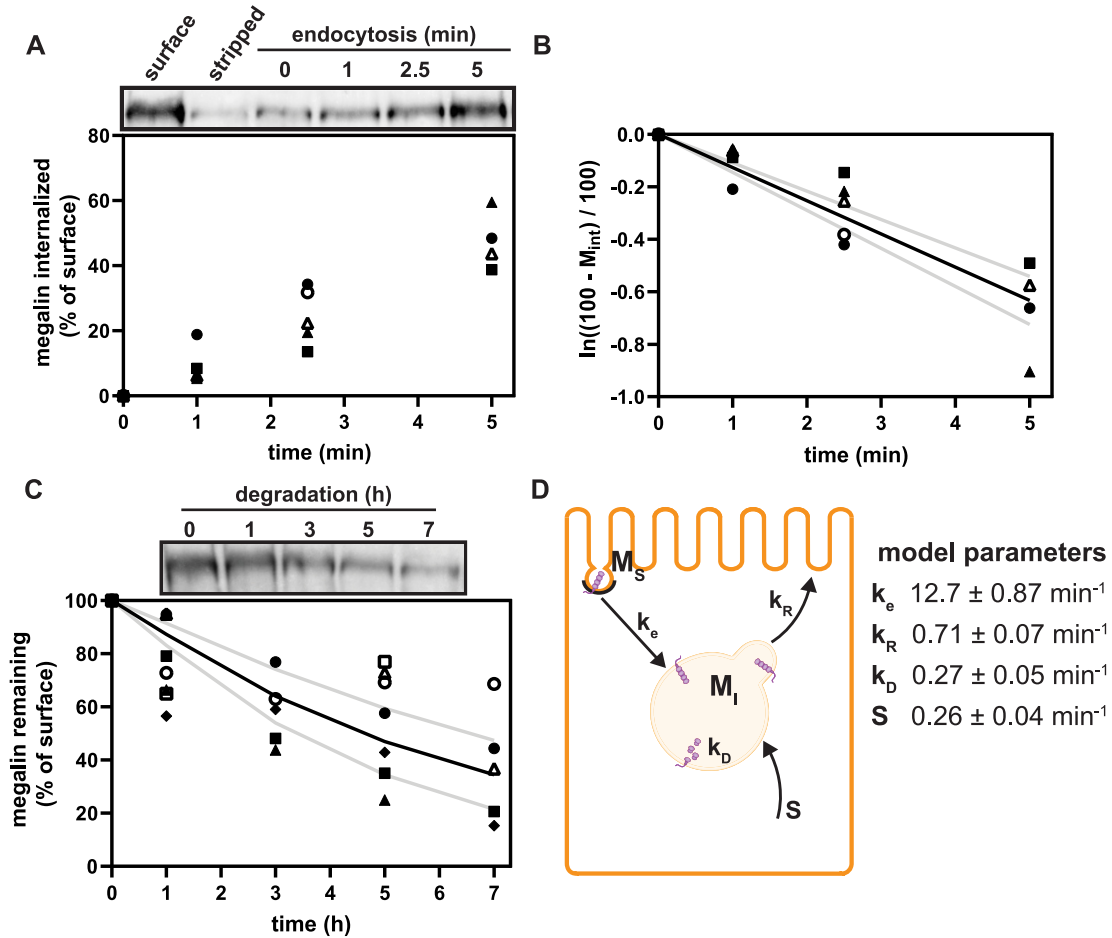
Figure 1. Preliminary model of megalin traffic based on biochemically measured parameters. (A) The apical surface of differentiated OK cells was biotinylated on ice, and cells were returned to culture for 0–5 min. One sample was stripped prior to return to culture as an added control ("stripped" lane). Biotin remaining at the apical surface was stripped at each time point and cells were solubilized. Biotinylated megalin was recovered using streptavidin beads and western blotted using antimegalin antibody. Internalized megalin was quantified as a percentage of the megalin at the surface at steady state. Data from 5 independent experiments are plotted and a representative blot showing a rapid increase in biotinylated megalin protected from stripping from 0 to 5 min is shown above the graph. (B) The % of surface megalin internalized over time in panel A was log transformed and fit to a line (black line) where the slope can be interpreted as the fractional endocytic rate (gray lines: 95% CI). (C) Degradation kinetics of apically biotinylated megalin in differentiated OK cells were quantified by returning biotinylated cells to culture for extended time periods. At each time point, cells were solubilized and recovered biotinylated megalin was blotted and quantified as a percentage of $T = 0$ h. Data from 7 independent experiments were used to fit (black line) the degradation rate of megalin using estimates of fractional endocytic rate (Figure 1B) and the fraction of megalin at the apical surface (see the "Materials and Methods" section; gray lines: 95% CI). A representative blot showing the decrease in biotinylated megalin over time is shown above the graph. (D) Diagram of a simple model of megalin traffic in OK cells based on surface biotinylation data. Megalin is divided into 2 pools: surface (M_S) and intracellular (M_I). Rates describing the trafficking between these pools were estimated from experimental data and are given as the % of megalin in the originating compartment (eg, surface or endosome) trafficked per minute. The synthesis (S) rate and degradation (k_D) rates represent the % of total megalin synthesized per minute and megalin in M_I that is degraded per minute, respectively.

general solution describing biotinylated megalin traffic, in terms of the kinetic parameters, is given by

$$\begin{bmatrix} M_S(t) \\ M_I(t) \end{bmatrix} = \left(\frac{100\lambda_2(\lambda_1 + k_D)}{k_D(\lambda_2 - \lambda_1)} \right) \begin{bmatrix} 1 \\ \frac{-\lambda_1}{k_D + \lambda_1} \end{bmatrix} e^{\lambda_1 t}$$

$$+ \left(100 - \frac{100\lambda_2(\lambda_1 + k_D)}{k_D(\lambda_2 - \lambda_1)} \right) \begin{bmatrix} 1 \\ \frac{-\lambda_2}{k_D + \lambda_2} \end{bmatrix} e^{\lambda_2 t} \quad (3)$$

and the eigenvalues of the system are defined as

$$\lambda_{1,2} = \frac{-k_e - k_R - k_D \pm \sqrt{k_e^2 + 2k_e k_R - 2k_e k_D + 2k_R k_D + k_R^2 + k_D^2}}{2}. \quad (4)$$

Estimation of Model Parameters
Parameters for the simple model of megalin traffic are fit entirely based on experimental data collected from surface biotinylation

assays. The fit kinetic parameter values with error are shown in Figure 1D.

Percent at Surface The steady-state value for % of megalin at the surface (M_S^s) is equivalent to the % at the surface estimated from the biotinylation assays.

Endocytic Rate The biotinylated megalin remaining at the surface during the brief endocytosis period can be represented as

$$M_S(t) = M_S(0)e^{(-k_e t)}, \quad (5)$$

where $M_S(t)$ is the biotinylated megalin remaining at the surface at time t and $M_S(0) = 100$. The data obtained from the endocytosis biotinylation assay (Figure 1A) represent the % of surface megalin that is internalized over time and is equivalent to $M_{int}(t) = M_S(0) - M_S(t)$. To estimate the endocytic rate of megalin,

the data from 0 to 5 min were log transformed and fit with a simple linear regression model such that

$$\ln\left(\frac{M_S(0) - M_{int}(t)}{M_S(0)}\right) = -k_e t. \tag{6}$$

The fit was performed using the fitnlm function in MATLAB R2021a and is shown in Figure 1B.

Recycling Rate Given the steady-state distributions defined in eqn (2), we can use the experimentally measured fraction at the surface and the endocytic rate to estimate the recycling rate

$$k_R = \frac{k_e M_S^*}{100 - M_S^*}. \tag{7}$$

Degradation Rate The surface biotinylation half-life data, which are the fraction of biotinylated megalin remaining over time following surface labeling and return to normal culture, can be described as $M_T(t) = M_S(t) + M_I(t)$. The degradation rate was estimated by fitting the general solution of the model, eqn (3), to the surface half-life data using the experimentally determined estimates of k_e and k_R. The fit was performed using the fitnlm function in MATLAB R2021a. Bootstrapping was used to estimate error for the fit k_D value. In brief, the half-life data were resampled 1000 times using the bootstrp function in MATLAB R2021a. The general solution was fit to each bootstrapped sample set to generate a distribution of k_D values. The error is SD of this distribution. The data and fit with error are shown in Figure 1C.

Synthesis Rate To maintain a nonzero steady state, the synthesis rate is equivalent to the amount of megalin degraded per unit time at steady state. Therefore, the synthesis rate can be estimated as

$$S = k_D \left(100 - M_S^*\right). \tag{8}$$

Recycling in Lifetime The average number of times a molecule of megalin recycles in its lifetime is

$$\bar{r} = \frac{1}{P_d}, \tag{9}$$

where P_d is the probability of degradation, which is defined as

$$P_d = \frac{k_d}{k_d + k_r}. \tag{10}$$

Expanded Model of Megalin Traffic Incorporating Biochemical and Colocalization Data

This model describes the trafficking of megalin in a PT cell based on experimental biochemical and colocalization data and is represented graphically in Figure 4A. At any given time, megalin is divided between the surface ($M_S(t)$) and the intracellular endocytic compartments, AEEs ($M_{AEE}(t)$), AVs ($M_{AV}(t)$), lysosomes ($M_{Lys}(t)$), and DATs ($M_{DAT}(t)$) such that the total amount of megalin is $M_T(t) = M_S(t) + M_{AEE}(t) + M_{AV}(t) + M_{Lys}(t) + M_{DAT}(t) = 100$.

The following system of ordinary differential equations describes the trafficking between these pools of megalin:

$$\frac{dM_S}{dt} = -k_e M_S + k_r M_{DAT}, \tag{11a}$$

$$\frac{dM_{AEE}}{dt} = k_e M_S - \left(k_{m,1} + k_{DAT,f}\right) M_{AEE}, \tag{11b}$$

$$\frac{dM_{AV}}{dt} = k_{m,1} M_{AEE} - \left(k_{m,2} + k_{DAT,s}\right) M_{AV} + S, \tag{11c}$$

$$\frac{dM_{Lys}}{dt} = k_{m,2} M_{AV} - k_d M_{Lys}, \tag{11d}$$

$$\frac{dM_{DAT}}{dt} = k_{DAT,f} M_{AEE} + k_{DAT,s} M_{AV} - k_r M_{DAT}, \tag{11e}$$

where k_e is the endocytic rate, k_r is the recycling rate from DATs, $k_{m,1}$ is the rate megalin "matures" from AEEs to AVs, $k_{DAT,f}$ is the rate megalin in AEEs is "sorted" into DATs, $k_{m,2}$ is the rate megalin "matures" from AVs to lysosomes, $k_{DAT,s}$ is the rate megalin in AVs is "sorted" into DATs, k_d is the degradation rate within lysosomes, and S is the synthesis rate.

To maintain consistency with the simple model, newly synthesized megalin must enter the pathway via an intracellular compartment. Based on previously described biosynthetic trafficking routes of apical proteins in polarized kidney cells, AVs were chosen as the best option for the entry point of newly synthesized megalin.[38]

At steady state (denoted by $*$), when all equations are set to zero, the distribution of megalin can be defined as

$$M_S^* = \frac{k_{DAT,s}\left(k_{DAT,f} + k_{m,1}\right) S}{k_e k_{m,1} k_{m,2}}, \tag{12a}$$

$$M_{AEE}^* = \frac{k_{DAT,s} S}{k_{m,1} k_{m,2}}, \tag{12b}$$

$$M_{AV}^* = \frac{S}{k_{m,2}}, \tag{12c}$$

$$M_{Lys}^* = \frac{S}{k_d}, \tag{12d}$$

$$M_{DAT}^* = \frac{k_{DAT,s}\left(k_{DAT,f} + k_{m,1}\right) S}{k_r k_{m,1} k_{m,2}}. \tag{12e}$$

Steady-State Distribution of Megalin From Colocalization Data

The steady-state distribution of megalin among the compartment defined earlier was estimated from the experimentally measured colocalization of megalin with markers for each compartment (Figure 2, Table S3) as well as the overlap between the markers themselves (Figure 3, Table S4). Additionally, we only consider DATs to be Rab11a-positive, since our colocalization data suggest that megalin is predominantly recycled through Rab11a- rather than Rab4-positive DATs. The steady-state % of megalin at the surface (M_S^*) comes directly from the biotinylation assays and is the same value as in the simple model. The percentage of megalin in the remaining compartments is defined as follows:

$$M_{AEE}^{\sim} = M_{EEA1}, \tag{13a}$$

$$M_{AV}^{\sim} = M_{Rab7}\left(1 - Rab7_{EEA1} - Rab7_{LysoTracker}\right), \tag{13b}$$

$$M_{Lys}^{\sim} = M_{LysoTracker}\left(1 - Lysotracker_{Rab11a}\right), \tag{13c}$$

$$M_{DAT}^{\sim} = M_{Rab11}\left(1 - Rab11a_{EEA1} - Rab11_{Rab7}\right), \tag{13d}$$

where $M^{\sim}$ is the uncorrected steady-state distribution of intracellular megalin. To ensure the sum of megalin in all compartments does not exceed 100%, the % in the intracellular compartments were adjusted by the factor x such that

$$100 = M_S^* + x\left(M_{AEE}^{\sim} + M_{AV}^{\sim} + M_{Lys}^{\sim} + M_{DAT}^{\sim}\right)$$
$$= M_S^* + M_{AEE}^* + M_{AV}^* + M_{Lys}^* + M_{DAT}^*. \tag{14}$$

The adjusted steady-state distribution of megalin with error is shown in Figure 4B.

Estimation of Model Parameters

Parameters for the expanded model of megalin traffic are fit based on experimental data collected from both the surface
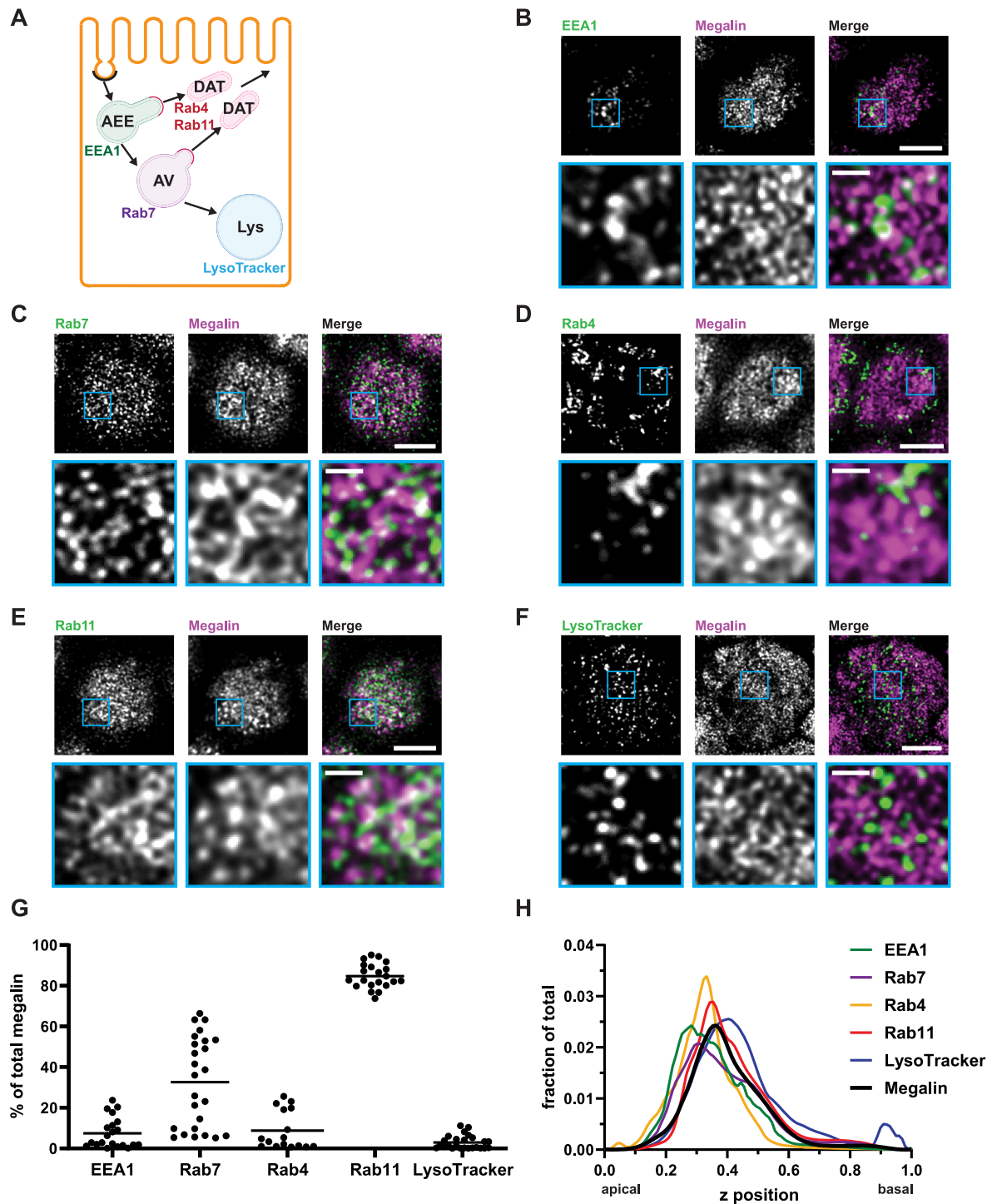
Figure 2. Steady-state distribution of intracellular megalin in OK cells. (A) Schematic of markers used to label endocytic compartments in PT cells: AEEs (EEA1), AVs (Rab7), DATs (Rab4 and Rab11a), and lysosomes (LysoTracker Red™). (B–F) OK cells on permeable supports were fixed and processed to detect megalin colocalization with the markers shown in panel A. Representative sum projection images of 6 planes were cropped to show a region of high colocalization of megalin with (B) EEA1, (C) Rab7, (D) Rab4, (E) Rab11a, and (F) LysoTracker Red within a single cell. Note the doming of the apical surface in these cells where subapical endocytic compartments are concentrated. Scale bars: 5 μm. Zoom-ins of selected areas are shown in blue boxes. Scale bars: 1 μm. (G) Megalin colocalization with each marker was quantified by Manders' coefficient over the entire z-stack and plotted as the % of total megalin. Each point represents a single z-stack image. (H) The average fractional distributions of EEA1 ($n = 111$), Rab7 ($n = 107$), Rab4 ($n = 61$), Rab11a ($n = 91$), LysoTracker ($n = 85$), and megalin ($n = 103$) over the z-axis of a cell, from 0 (apical) to 1 (basal), are plotted. Individual curves with SEM for each marker are shown in Figure S2.
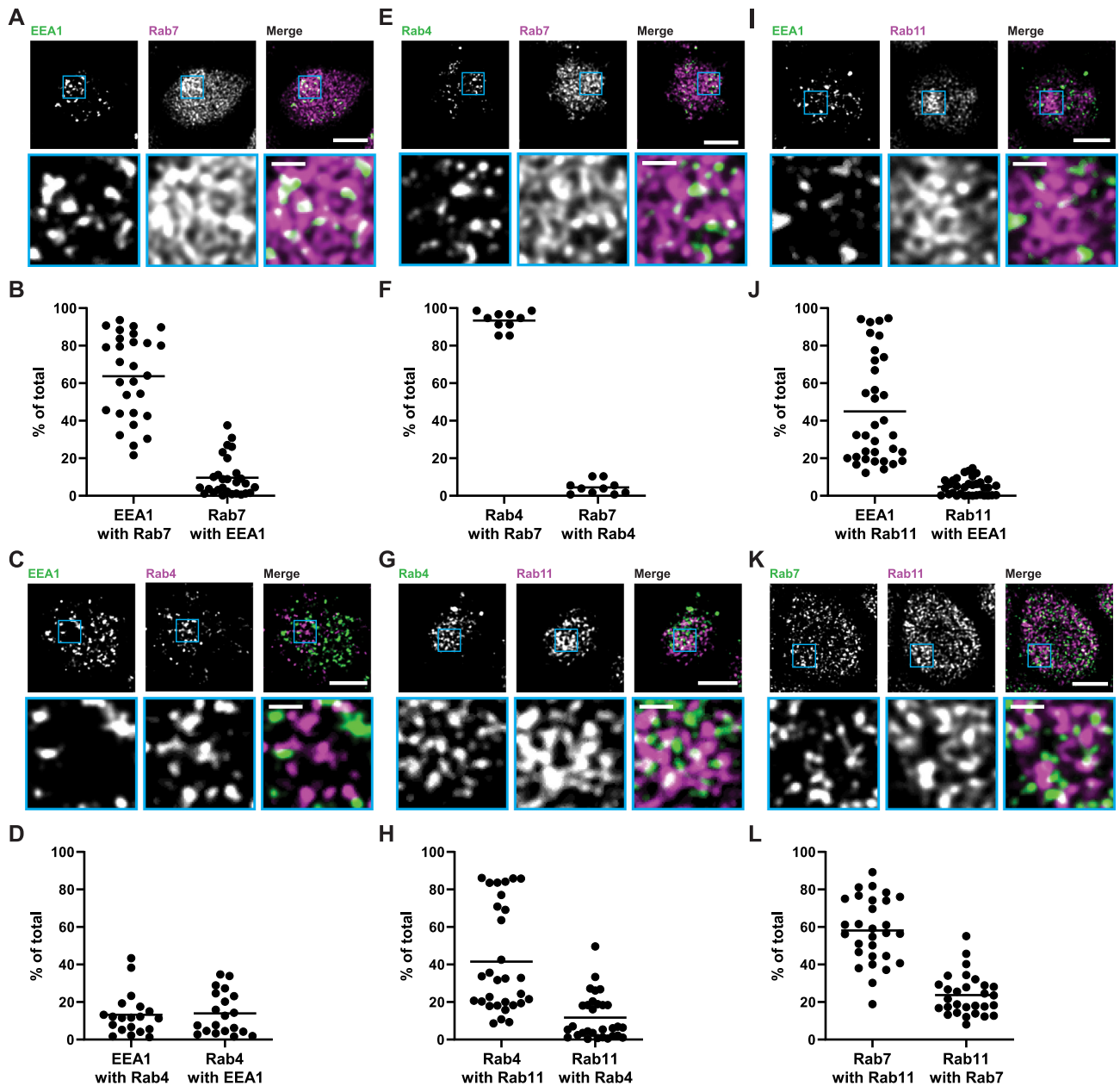
Figure 3. Quantitation of the overlap between endocytic markers in OK cells. OK cells on permeable supports were fixed and processed to detect colocalization between the indicated pairs of endocytic compartment markers (A and B) EEA1 and Rab7, (C and D) EEA1 and Rab4, (E and F) Rab4 and Rab7, (G and H) Rab4 and Rab11a, (I and J) EEA1 and Rab11a, and (K and L) Rab7 and Rab11a. Representative sum projection images of 6 planes were cropped to show a region of high colocalization between the markers (A, C, E, G, I, and K). Scale bars: 5 μm. Zoom-ins of selected area are shown in blue boxes. Scale bars: 1 μm. Quantification by Manders' coefficient over the entire z-stack, shown as the % of total is shown below each set of images (B, D, F, H, J, and L). Each point represents a single z-stack image.

biotinylation assays and quantitative colocalization. The fit kinetic parameter values with error are shown in Figure 4C.

Endocytic Rate The endocytic rate for the expanded model is equivalent to the experimentally measured endocytic rate used in the simple model (k_e).

Degradation Rate The amount megalin degraded per unit time in the expanded model is equivalent to amount of megalin degraded per unit time in the simple model, $k_d M_{Lys}^* = k_D M_I^*$. Therefore, the degradation rate in the expanded model, k_d, can

be defined as

$$k_d = \frac{k_D \left(100 - M_S^*\right)}{M_{Lys}^*}. \tag{15}$$

Synthesis Rate The synthesis rate is equal to the amount of megalin degraded per unit time and is equal to synthesis estimated in the simple model (S).

Intracellular Trafficking Rates The intracellular trafficking rates, $k_{m,2}$ and k_r, can be defined in terms of the steady-state distribution of megalin and experimentally determined kinetic rates
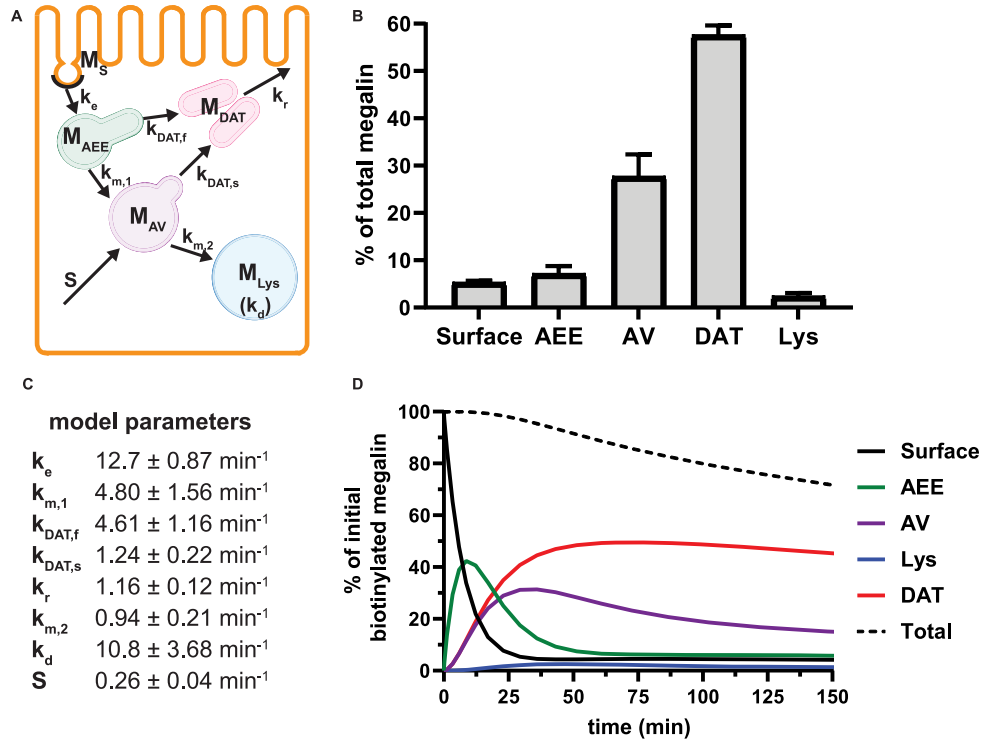
Figure 4. Comprehensive model of megalin traffic incorporating quantitative biochemical and imaging data. (A) Graphical representation of the model of megalin traffic displaying endosomal compartments with coefficients denoting the kinetic rates of megalin traffic between these compartments. (B) Megalin steady-state distribution among the endocytic compartments, surface, AEEs, AVs, DATs, and lysosomes (Lys), (mean ± SEM), which was calculated as described in the "Materials and Methods" section based on the average fractional colocalization of megalin with each marker in Figure 2 and the overlaps between the markers in Figure 3. (C) Kinetic trafficking rates between these endosomal compartments were estimated from experimental data and are given as the % of megalin in the originating compartment (eg, surface or endosome) trafficked per minute. The synthesis (S) rate and degradation (k_D) rates represent the % of total megalin synthesized per minute and megalin in M_{lys} that is degraded per minute, respectively. (D) The predicted temporal route of megalin biotinylated at the apical surface through each compartment is plotted. In this simulation, the synthesis rate is set to zero since no newly biotinylated megalin is created after initial labeling. The total remaining biotinylated megalin over time is plotted as the black dashed line.

:

$$k_{m,2} = \frac{S}{M_{AV}^*}, \quad (16)$$

$$k_r = \frac{k_e M_S^*}{M_{DAT}^*}. \quad (17)$$

The rates $k_{m,1}$, $k_{DAT,f}$, and $k_{DAT,s}$ are dependent on one another and on the amount of megalin recycled. The amount of megalin recycled is equivalent to the megalin entering DATs:

$$k_r M_{DAT}^* = k_{DAT,f} M_{AEE}^* + k_{DAT,s} M_{AV}^*. \quad (18)$$

Assuming megalin enters DATs through both the slow and fast pathways

$$k_{DAT,f} M_{AEE}^* = (1 - \alpha) k_r M_{DAT}^*, \quad (19)$$

$$k_{DAT,s} M_{AV}^* = \alpha k_r M_{DAT}^*, \quad (20)$$

where $0 < \alpha < 1$. We can define maturation from AEE to AVs, $k_{m,1}$, in terms of experimentally determined values and $k_{DAT,f}$

$$k_{m,1} = \frac{k_e M_S^* - k_{DAT,f} M_{AEE}^*}{M_{AEE}^*}. \quad (21)$$

Given experimental estimates of the steady-state distribution and eqn (17), eqns (19) and (20) can be used to estimate $k_{DAT,f}$ and $k_{DAT,s}$ if we assume a value for α. From our colocalization data, we found that a higher fraction of Rab11a colocalizes with Rab7 than EEA1 and that the z-distributions of megalin and Rab11a align more closely with that of Rab7 than EEA1. Given these observations, we assume a larger fraction of recycling megalin traffics through AVs than AEEs. Because we

lack quantitative measurements to describe the fraction of recycling megalin entering DATs from AVs, for further investigations with this model, we assumed 51% of recycling megalin traffics through AVs ($\alpha = 0.51$). Figure S3A demonstrates how the values of $k_{m,1}$, $k_{DAT,f}$, and $k_{DAT,s}$ change with the fraction of recycled megalin from AVs (α). Figure S3B shows the predicted trajectory of apically biotinylated megalin when we assume that a much higher fraction of megalin recycles from AVs ($\alpha = 0.8$). Increasing the fraction of megalin recycling from AVs, results in a more rapid rise in the fraction of megalin in AVs and a more gradual rise in the fraction of megalin in DATs.

Model of Megalin Traffic in Mouse S1 PT Cells

This model describes the trafficking of megalin in a mouse S1 PT cell based on experimental colocalization data and is represented graphically in Figure 6D. At any given time, megalin is divided between the surface ($M_S(t)$) and the 2 intracellular pools, megalin available for recycling ($M_E(t)$) and lysosomes ($M_{Lys}(t)$), such that the total amount of megalin is $M_T(t) = M_S(t) + M_E(t) + M_{Lys}(t) = 100$. Due to high degree of overlap between endocytic markers EEA1, Rab7, and Rab11, we cannot distinguish between megalin in AEEs, AVs, or DATs. Therefore, the megalin in these compartments is grouped into one pool, megalin available for recycling ($M_E(t)$).

The following system of ordinary differential equations describe the trafficking between these pools of megalin:

$$\frac{dM_S}{dt} = -k_e M_S + k_{rec} M_E, \tag{22a}$$

$$\frac{dM_E}{dt} = k_e M_S - (k_{mat} + k_{rec}) M_E + S, \tag{22b}$$

$$\frac{dM_{Lys}}{dt} = k_{mat} M_E - k_d M_{Lys}, \tag{22c}$$

where k_e is the endocytic rate, k_r is the recycling rate, k_{mat} is the rate intracellular megalin "matures" to lysosomes, k_d is the degradation rate within lysosomes, and S is the synthesis rate.

At steady state (denoted by ∗), when all equations are set to zero, the distribution of megalin can be defined as

$$M_S^* = \frac{k_{rec} S}{k_e k_{mat}}, \tag{23a}$$

$$M_E^* = \frac{S}{k_{mat}}, \tag{23b}$$

$$M_{Lys}^* = \frac{S}{k_d}. \tag{23c}$$

The % of megalin at the surface (M_S^*) and in lysosomes (M_{Lys}^*) at steady state is determined from the quantitative colocalization of megalin with SGLT2 and LAMP1, respectively (Figure 6). The remaining % of total megalin is the megalin available for recycling, $M_E^* = 100 - M_S^* - M_{Lys}^*$.

Though we lack kinetic data in mouse, we can still determine the endocytic-to-recycling rate ratio for megalin

$$\frac{k_e}{k_{rec}} = \frac{M_S^*}{100 - M_S^* - M_{Lys}^*}. \tag{24}$$

We can also determine the relative amount of megalin that matures lysosomes to the megalin degraded in lysosomes per minute:

$$\frac{k_{mat}}{k_d} = \frac{M_{Lys}^*}{100 - M_S^* - M_{Lys}^*}. \tag{25}$$

These ratios can be compared with those of the OK cells, when megalin traffic is described in the same way. It should be noted that this recycling rate, k_{rec}, is not equivalent to either k_R in the preliminary or k_r in the expanded OK cell models.

Propagation of Error

Where necessary, the error for model parameters was estimated using these error propagation rules.

When $Q = a + b$, the error of Q can be estimated as

$$\delta Q = \sqrt{\delta a^2 + \delta b^2}. \tag{26}$$

When $Q = ab$, the error of Q can be estimated as

$$\delta Q = \sqrt{\left(\frac{\delta a}{|a|}\right)^2 + \left(\frac{\delta b}{|b|}\right)^2}. \tag{27}$$

Steady-State Sensitivity Application

Using the application compiler in MATLAB R2021a, we developed a downloadable stand-alone application that outputs the steady-state distribution of megalin and can be run from the command line. The application takes inputs of kinetic trafficking parameters and using eqns (12a)–(12e), outputs the steady-state distribution of megalin as a percentage of total. Installation and use instructions are provided in the Supplementary Materials. Link to download: https://github.com/keshipman/Model-of-megalin-traffic-in-OK-cells

Results

Trafficking Kinetics of Surface Megalin

To quantify the trafficking kinetics of megalin in differentiated OK cells, megalin at the apical surface was labeled by surface biotinylation. The percentage of total megalin localized to the apical surface was calculated by comparison with total cell lysate. Consistent with previous reports in rodent PT,[39,40] most megalin in OK cells is intracellular at steady state, with only 5.29% (SEM: 0.38, $n = 9$) localized to the apical surface. Next, we quantified endocytic kinetics of megalin over a short time course (Figure 1A). We found that megalin is rapidly endocytosed from the apical surface, with nearly 50% of the initially biotinylated megalin internalized within 5 min. These data were log-transformed as described in the "Materials and Methods" section and fit by linear regression, where the absolute value of the slope is equivalent to the fractional endocytic rate of surface megalin (Figure 1B, k_e in Figure 1D). We also quantified the half-life of megalin biotinylated at the apical membrane upon returning the cells to culture (Figure 1C). These studies confirmed that megalin is a long-lived receptor, with a half-life of ∼5.7 h.

We used this biochemical data to construct a preliminary kinetic model of megalin traffic as described in the "Materials and Methods" section. A graphical representation with fit rates is shown in Figure 1D. In this model, megalin is divided into surface (M_S) and intracellular (M_I) pools, with kinetic rates that describe the traffic between them. Surface megalin is internalized at endocytic rate k_e into the intracellular pool. Intracellular megalin is either recycled back to the surface at rate k_R or degraded at rate k_D. Newly synthesized megalin (S) enters the system through the intracellular pool, based on previous studies demonstrating that newly synthesized apically destined proteins in kidney cells transit endocytic compartments.[38] The recycling rate was estimated based on k_e and the steady-state percentage at the apical surface designated M_S^*. The degradation rate was determined by fitting the solution to this model to the surface half-life data using our experimentally measured k_e and estimated k_R as described in the "Materials and Methods" section. With experimental estimates of k_e and k_R and the fit value of k_D, the solution with t in minutes and $M_S(t)$ and $M_I(t)$ as a % of initial biotinylated megalin is

$$\begin{bmatrix} M_S(t) \\ M_I(t) \end{bmatrix} = 5.499 \begin{bmatrix} 1 \\ 17.54 \end{bmatrix} e^{-0.0026t} + 94.50 \begin{bmatrix} 1 \\ -1.021 \end{bmatrix} e^{-0.1338t}. \tag{28}$$

This fit is shown in Figure 1C. The synthesis rate was set equal to the % of total megalin degraded per minute at steady state ($k_D M_I^*$). This model predicts that the endocytic rate is much faster than the recycling rate, and that the recycling rate is considerably greater than the degradation rate of intracellular megalin. Based on our fit and estimated values, a molecule of megalin is predicted to be internalized and recycled on average 3.6 times in its lifetime.

Distribution of Intracellular Megalin

Recycling of megalin in PT cells has been suggested to occur from early endosomes and AVs via fast and slow recycling, respectively. In order to refine our model, we quantified the intracellular distribution of megalin relative to markers of endocytic compartments. Differentiated OK cells were co-stained to label megalin and predicted markers of AEEs (EEA1), AVs (Rab7), DATs (Rab4 and Rab11a), and lysosomes (LysoTracker dye) (Figure 2A–F). These markers were selected based on studies in

cell lines with well-established endocytic pathways.[41–43] Anti-EEA1- and Rab7-antibodies and LysoTracker labeled primarily punctate structures consistent with their localization to maturing endosomal structures and lysosomes, respectively. In contrast, Rab11a antibodies labeled a network of tubular structures that were closely apposed to EEA1- and Rab7-positive compartments. Rab4 labeled clusters of structures were often located at the cell periphery. The colocalization of megalin with each marker was quantified by Manders' coefficient to provide the fraction of total megalin associated with each compartment (Figure 2G and Table S3). A large fraction of megalin colocalized with Rab11a, and considerable overlap was also detected with Rab7. In contrast, very little megalin colocalized with EEA1 and Rab4. As expected, there was virtually no colocalization of megalin with LysoTracker.

To better understand how these endocytic markers and megalin are distributed, we quantified their average fractional distribution over the z-axis, or height of the cell (Figure 2H, Figures S1 and S2). The positions of each marker distribution maximum are consistent with the expected trajectory of the endocytic pathway, with peak of the EEA1 distribution occurring first, followed by Rab7, and then Lysotracker along the z-axis. Most of the recycling markers (Rab4 and Rab11a) are between Rab7 and LysoTracker maximums, with Rab4 more apically distributed than Rab11a. The distribution of megalin corresponds directly with that of Rab11a. This region also overlaps with the majority of the Rab7 distribution rather than with EEA1.

Overlap Between Endocytic Compartment Markers

The sum of total megalin colocalizing with each compartment marker in Figure 2G is greater than 100%, as would be expected if there is overlap between the markers themselves. To deconvolute these relationships, we co-stained differentiated OK cells to label different combinations of endocytic markers and quantified the overlap by Manders' coefficient (Figure 3 and Table S4). A large percentage of EEA1 overlapped with Rab7 (Figure 3A and B), suggesting that AEEs are rapidly maturing into AVs in our cells. Surprisingly, we found very little Rab4 overlapping with EEA1; rather the majority of Rab4 colocalized with both Rab7 and Rab11a (Figure 3C–F). These data are inconsistent with the previous assumption in MDCK cells of a Rab4-driven "fast recycling" pathway from early endosomal compartments in OK cells.[18] There was considerable overlap of EEA1 and Rab7 with Rab11a, suggesting that Rab11a-positive DATs form from both EEA1- and Rab7-positive compartments (Figure 3I–L). This finding, together with our megalin colocalization data (Figure 2), lead us to conclude that Rab11a, rather than Rab4, is the primary marker for DATs and plays a primary role in megalin recycling from both AEEs and AVs. Additionally, because megalin colocalizes preferentially with Rab7 over EEA1 (Figure 2), and because there is greater overlap of Rab7 with Rab11a (Figure 3L) than of EEA1 with Rab11a (Figure 3C), we conclude that the majority of megalin enters DATs from AVs rather than AEEs. This would be expected if endosome maturation occurs very rapidly in PT cells. We observed a higher degree of variability in our measurement of megalin colocalization with Rab7 than with other markers (Figure 2G). We believe that this reflects subtle differences in the rapid rate of endosome maturation due to slight variations in experimental conditions, especially since we observe a similar degree of variability when examining the overlap between EEA1 and Rab7 (Figure 3B).

Mathematical Model of Megalin Traffic

Using our colocalization data, we refined our mathematical model of megalin traffic to incorporate rates for megalin trafficking between intracellular compartments in OK cells. A graphical representation of the expanded model is shown in Figure 4A. In this model, surface megalin is internalized at endocytic rate k_e into AEEs. Megalin remains in AEEs maturing to AVs at rate k_{m1} or enters DATs through the fast-recycling route at rate $k_{DAT,f}$. From AVs, megalin enters DATs through the slow-recycling route at rate $k_{DAT,s}$ or is delivered to lysosomes at rate k_{m2}. Megalin within DATs is recycled to the apical surface at rate k_r. Megalin within lysosomes is degraded at rate k_d. Newly synthesized megalin (S) enters the system through AVs. The steady-state distribution of megalin among model compartments was calculated based on the average % of megalin at apical surface quantified in our biotinylation assays and its colocalization with each intracellular compartment marker.

To avoid counting megalin more than once in regions that contain marker overlap, we combined data from megalin colocalization with compartment markers in Figure 2 and the colocalization data between pairs of markers measured in Figure 3 to establish the intracellular distribution of the receptor. The calculations used to determine the steady-state distribution of megalin are described in detail in the "Materials and Methods" section. The resulting distribution of megalin between the apical surface and endocytic compartments, plotted as a % of the total, is shown in Figure 4B. At steady state, more than half (57.6%) of the total megalin is localized to DATs. The next highest fraction of total megalin (27.7%) is localized to AVs, while much smaller fractions are localized to the surface (5.29%), AEEs (7.12%), and lysosomes (2.39%).

We solved the model equations at steady state to define steady-state distributions in terms of the kinetic rates. With rearrangement, the intracellular trafficking rates can be defined in terms of the experimentally measured rates (endocytosis and degradation of surface megalin) and the steady-state distribution as described in detail in the "Materials and Methods" section. The intracellular trafficking rates k_{m1}, $k_{DAT,f}$, and $k_{DAT,s}$ are dependent on one another, which precludes estimating their values from the steady-state distribution of megalin alone. We therefore included an additional parameter α, which describes the fraction of recycling megalin that traffics through AVs or recycles "slowly," in order to estimate values for k_{m1}, $k_{DAT,f}$, and $k_{DAT,s}$. Figure S3A shows how these parameters are linearly dependent on the value of α, with k_{m1} and $k_{DAT,s}$ increasing and $k_{DAT,f}$ decreasing with increasing α. From our colocalization data, we concluded that a larger fraction of megalin enters DATs from AVs rather than AEEs, but we lack quantitative measurements to experimentally determine the precise value. For further investigations with this model, we made the conservative assumption that 51% of recycling megalin traffics through AVs ($\alpha = 0.51$). The estimated kinetic rates, calculated as the percentage of megalin in each originating compartment that is "trafficked" per minute, are shown in Figure 4C. For S and k_d, these values denote the fraction of total megalin synthesized per minute and the fraction in lysosomes that is degraded every minute, respectively. Table S5 shows these rates as number of megalin molecules trafficked per minute for every 10,000 molecules of megalin in the cell.

As predicted from our colocalization data, the rates of megalin exit from AEEs (k_{m1} and $k_{DAT,f}$) are very fast, which suggest that these compartments are short-lived. Recycling from

the DATs to the surface (k_r) is considerably slower, which indicates that megalin has a long residence time in DATs. Figure 4D tracks the predicted temporal distribution of megalin molecules biotinylated at the apical plasma membrane at time 0 min. Megalin is rapidly internalized from the surface and this pool accumulates in AEEs, such that more than 40% of the biotinylated megalin is present in AEEs after 10 min. Following this peak in the fraction of megalin within AEEs, there is a rapid, almost simultaneous, rise in the fraction of megalin in AVs and DATs. The fraction in AVs slowly declines as more megalin enters DATs. Altering our assumption regarding the fraction of megalin entering DAT from AVs (α) so that more megalin recycles from the "slow" pathway, results in a greater accumulation of megalin in AVs at 25 min and delays the rise in the fraction of megalin in DATs (Figure S3B). However, it does not impact the rapid rise and fall of the fraction of megalin in AEEs. Given the rapid endocytic rate and large fraction of total megalin in DATs at steady state, this model suggests that the recycling rate is the rate limiting step in determining the amount of megalin at the surface and consequently the maximum endocytic capacity of PT cells.

To test the robustness of our model, we determined the sensitivity of the predicted kinetic rates to experimentally measured values. The percentage of megalin at the apical surface (M_S^*) and fractional endocytic rate (k_e) are necessary measurements to determine all other trafficking rates. To determine the effect of experimental variability on our model predictions, we adjusted the measured values of these parameters by a factor of 0.5–2 and recalculated the kinetic rates keeping all else the same (Figure S4). Figure S4A shows how each predicted rate changed when we individually varied k_e and M_S^*. The rates that were most substantially affected by changes in k_e or M_S^* were $k_{m,1}$ and $k_{DAT,f}$, which increased linearly with both k_e and M_S^*. Since raising either k_e or M_S^* increases the amount of megalin internalized per unit time, it makes sense that predicted values of both AEE maturation ($k_{m,1}$) and fast recycling ($k_{DAT,f}$) increased proportionally to maintain the relatively low fraction of total megalin we observed within AEEs. As expected, there is an even greater effect on these parameters when both k_e and M_S^* are increased together (Figure S4B).

To test the model's usefulness in predicting how alterations in trafficking can affect the endocytic capacity of PT cells, we performed a sensitivity analysis of the steady-state distribution of megalin in response to changes in kinetic trafficking rates (Figure 5, Figure S5). Because the amount of megalin at the surface dictates the endocytic capacity of the cell, we focused our analysis on how altering kinetic rates affects this parameter. Altering k_e had the largest effect on the fraction of megalin at the surface, with a nearly 2-fold increase in surface megalin predicted when the endocytic rate was reduced by half (Figure 5A). However, because the reduction in k_e compensates for the increase in the fraction of megalin at the surface, varying k_e had little effect on the fraction of total megalin that was internalized per unit time.

Altering the intracellular trafficking rates also affected the fraction of megalin at the surface. Figure 5B shows the effect on surface megalin when maturation and recycling rates were individually varied. In these instances, without changes in k_e, the change in fraction of total megalin internalized per unit time is proportional to the change in the fraction of megalin at the surface. Of the intracellular trafficking rates, the rate of recycling from DATs to the surface, k_r, has the largest impact on the fraction of megalin at the surface (Figure 5B, red line). Increasing k_r and k_e together had opposing effects on the fraction at the surface (Figure 5A). However, the effect on the fraction of megalin
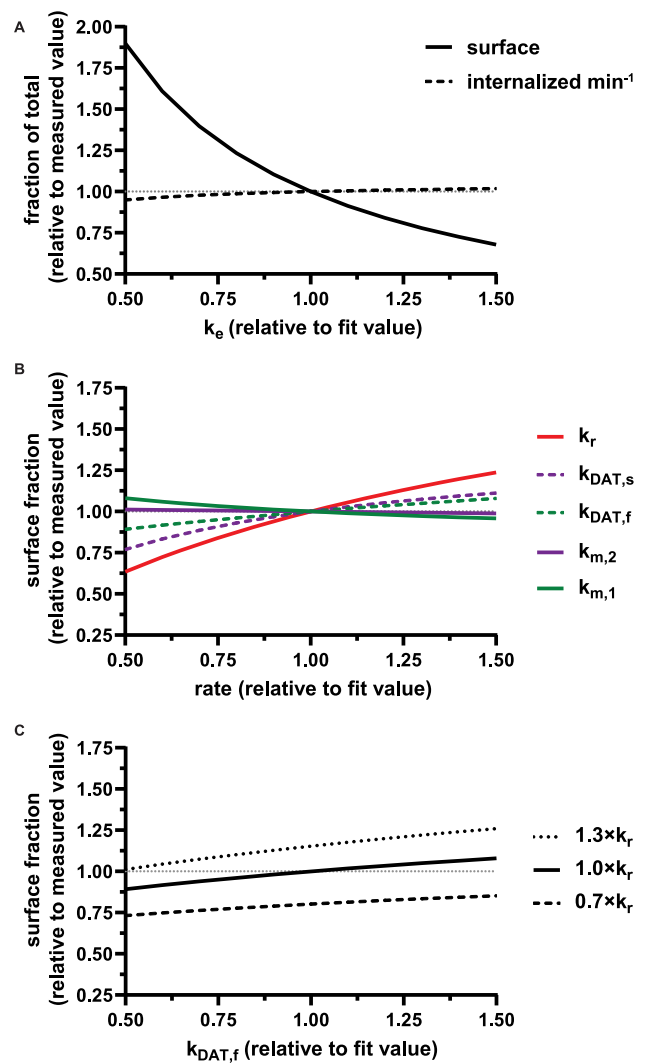

Figure 5. Sensitivity of the percentage of megalin at apical surface in response to changes in kinetic trafficking rates. (A) The fraction of total megalin at the surface (solid line) or internalized per minute (dashed line) in response to changes in the endocytic rate, k_e. k_e is plotted relative to the fit value provided in Figure 4C (1.00 on x-axis). The fraction of total megalin is plotted relative to the measured value (M_S^*, 5.29%; represented by the dotted line at 1.0 on the y-axis in all panels). The fraction of total megalin internalized per minute was determined by multiplying the new k_e by the new fraction at the surface and is plotted relative to this rate using the fit k_e and measured M_S^*. Note that changes in k_e have significant effects on the steady-state level of megalin at the apical surface but minimal effects on the fraction of total megalin internalized per minute. (B) The fraction of total megalin at the surface in response to changes in the intracellular trafficking rates, $k_{m,1}$, $k_{DAT,f}$, $k_{DAT,s}$, k_r, and $k_{m,2}$. The rates are plotted relative to the fit values provided in Figure 4C. The fraction of total megalin is plotted relative to the measured value. (C) The fraction of total megalin at the surface in response to changes in $k_{DAT,f}$ with a relative to the fit value in Figure 4C, and the fraction of total megalin is plotted relative to the measured value.

internalized per unit time was essentially equivalent to altering k_r alone (Figure S5A). Outside of k_r, the entry rates into DATs, $k_{DAT,f}$ and $k_{DAT,s}$, had the next largest effects on the fraction of megalin at the surface (Figure 5B). These rates directly dictate how much megalin is available for recycling. When $k_{DAT,f}$ and k_r were varied together, to simulate an overall change in fast recycling, there was a greater effect on the fraction of megalin at the surface (Figure 5C). In contrast, altering exit rates from AEEs

($k_{m,1}$ and $k_{DAT,f}$) concurrently had almost no effect on the fraction of megalin at the surface (Figure S5B). Changing both entry rates into DATs ($k_{DAT,f}$ and $k_{DAT,s}$) simultaneously resulted in a greater effect than altering each one alone, however, the overall effect on the fraction of megalin at the surface was less than that of altering k_r alone (compare Figure S5C to Figure 5B, red line). Overall, our analysis demonstrates that the rates determining how much megalin is recycled ($k_{DAT,f}$, $k_{DAT,s}$, and k_r) have the largest impact on the steady-state fraction of megalin at the surface. For further investigation on the steady-state distribution of megalin in response to changes in kinetic rates, we developed a stand-alone application that will provide the steady-state distribution of megalin across all compartments given user-supplied kinetic rates as inputs (see the "Materials and Methods" section and Supplementary Material).

A Model for Megalin Traffic in Mouse Kidney

Based on their overall transcriptional profile, differentiated OK cells are most representative of the S1 segment of the PT.[27–30] Based on previously published transcriptomic and digital droplet PCR data, we estimated that S1 cells in mouse kidney express ~3 times more megalin than OK cells.[30,44] Biochemical measurements necessary to quantify megalin endocytosis and half-life in these cells cannot be obtained in living animals, so we adapted our model to estimate in vivo kinetic rates using colocalization data of megalin with surface and intracellular markers in mouse kidney S1 segments. Fixed kidney sections were co-stained to label megalin, the S1 segment marker SGLT2, and EEA1, Rab7, Rab11, or LAMP1. In addition to identifying S1 segments, SGLT2 staining was used to localize the apical membrane since it has a strong brush border distribution.[45] A representative image of an end-on tubule showing megalin co-stained with anti-SGLT2 and anti-LAMP1 antibodies to denote the beginning and end of the endocytic pathway, respectively, is shown in Figure 6A. Megalin colocalization with SGLT2, EEA1, Rab7, Rab11, and LAMP1 was quantified by Manders' coefficient (Figure 6B). Consistent with our findings in OK cells, only a small fraction of megalin colocalized with SGLT2 at the apical surface (7.75%), while a much larger fraction colocalized with Rab11 (66.2%). However, in contrast to our staining in planar OK cell cultures, we were unable to confidently distinguish between megalin in sorting versus recycling endocytic compartments in kidney tubules, as there was an extensive overlap of megalin with EEA1 and Rab7, as well as between EEA1, Rab7, and Rab11a with each other (Figure 6B, Figure S6). Therefore, we constructed an abridged model of megalin traffic in mouse S1 cells, in which megalin is divided into a surface pool (M_S), an intracellular pool within endosomes still accessible for recycling (M_E), and a lysosomal pool (M_{Lys}) (Figure 6C). In this model, surface megalin is internalized at rate k_e into the intracellular, recycling available pool, which includes megalin in AEES, AVs, and DATs. From there, megalin is recycled at rate k_{rec} or matures to lysosomes at rate k_{mat}. In lysosomes, megalin is degraded at rate k_d. Newly synthesized megalin (S) enters the system through the recycling available pool. We estimated the steady-state distribution of megalin using our colocalization of megalin with SGLT2 and LAMP1. Without direct measurements of megalin endocytic or degradation kinetics in vivo, we assumed the same fractional endocytic rate (k_e) and the same fractional degradation rate in lysosomes (k_d) as we measured in OK cells.

Figure 6C compares megalin distribution and traffic in an OK cell versus mouse S1 PT cell in terms of megalin molecules for every 10,000 molecules in each cell type. The higher fraction of megalin at the apical surface of mouse S1 segments compared with OK cells suggests that endocytic flux in vivo is more rapid than in our cell culture model. Assuming the fractional endocytic rate of megalin is the same as (or greater than) in OK cells, the fractional recycling rate of megalin is about 1.7 times faster in mouse than in OK cells. The higher fraction of megalin in lysosomes in mouse S1 segments indicates that endosome maturation is also more rapid than in OK cells. Figure 6D tracks the predicted temporal distribution of megalin molecules at the apical plasma membrane at time 0 min in OK cells and in the mouse S1 segment. In both, megalin is rapidly internalized from the surface, and this pool accumulates in endosomes where megalin is then recycled back to the surface or trafficked to lysosomes. The accumulation of megalin from the initial surface pool in endosomes peaks at ~20 min in both OK and mouse cells. The flux through recycling compartments is more rapid in mouse as shown by the more rapid decline of megalin from the initial pool in this compartment compared to OK cells.

Discussion

Here, we utilized an optimized OK cell culture model to conduct an in-depth study of the organization of the PT apical endocytic pathway and the trafficking of megalin receptors through these compartments. Key elements of this model were adapted to estimate megalin kinetic trafficking parameters in the mouse PT S1 segment. Our study provides the first quantitative description of the steady-state distribution and kinetic trafficking rates of megalin in a PT specific cell line and clarifies the critical steps that underlie the ability of PT cells to maintain the rapid flux necessary to continuously recover a large number of ligands from the ultrafiltrate.

Our biochemical and morphological data indicate that the majority of megalin is localized to intracellular compartments at steady state (~94% in OK cells and ~89% in mouse S1 cells). Prior studies in rodents have qualitatively observed lower levels of megalin staining at the brush border compared to the subapical region in the S1 segment of the PT.[39,40] This distribution is perhaps counterintuitive for a receptor that functions at the plasma membrane, but in fact the small fraction of megalin at the apical surface reflects its very rapid internalization rate (12.7% min^{-1}). This rapid internalization in PT cells likely facilitates the efficiency of recovery of ligands with low binding affinities for the multiligand receptors to prevent their excretion in the urine. This is in stark contrast to the distribution and trafficking of heterologously expressed tagged truncated megalin in MDCK cells.[21] In MDCK cells, nearly all of the megalin (83%) is localized to the apical surface at steady state as quantified by surface biotinylation, and the estimated fractional endocytic rate was substantially lower than our estimates in differentiated OK cells (3% min^{-1}; reported as $k_{01} = .001\,s^{-1}$ with total = 2.0). These differences in megalin distribution and internalization likely reflect the very different organization of the apical endocytic pathway in MDCK versus OK cells and emphasizes the importance of studying megalin traffic in a cell line that approaches in vivo PT function and morphology.

Our data suggest that megalin recycling is primarily dependent on Rab11a rather than on Rab4. Nearly 85% of the total megalin colocalized with Rab11a, which labels a dense network of apical tubular structures in our cells that appear to emanate from both EEA-positive and Rab7-positive endosomes, which aligns with previous morphological studies demonstrating that DATs originate from both AEEs and AVs.[16,17] In contrast, very little megalin colocalized with the canonical "fast recycling"
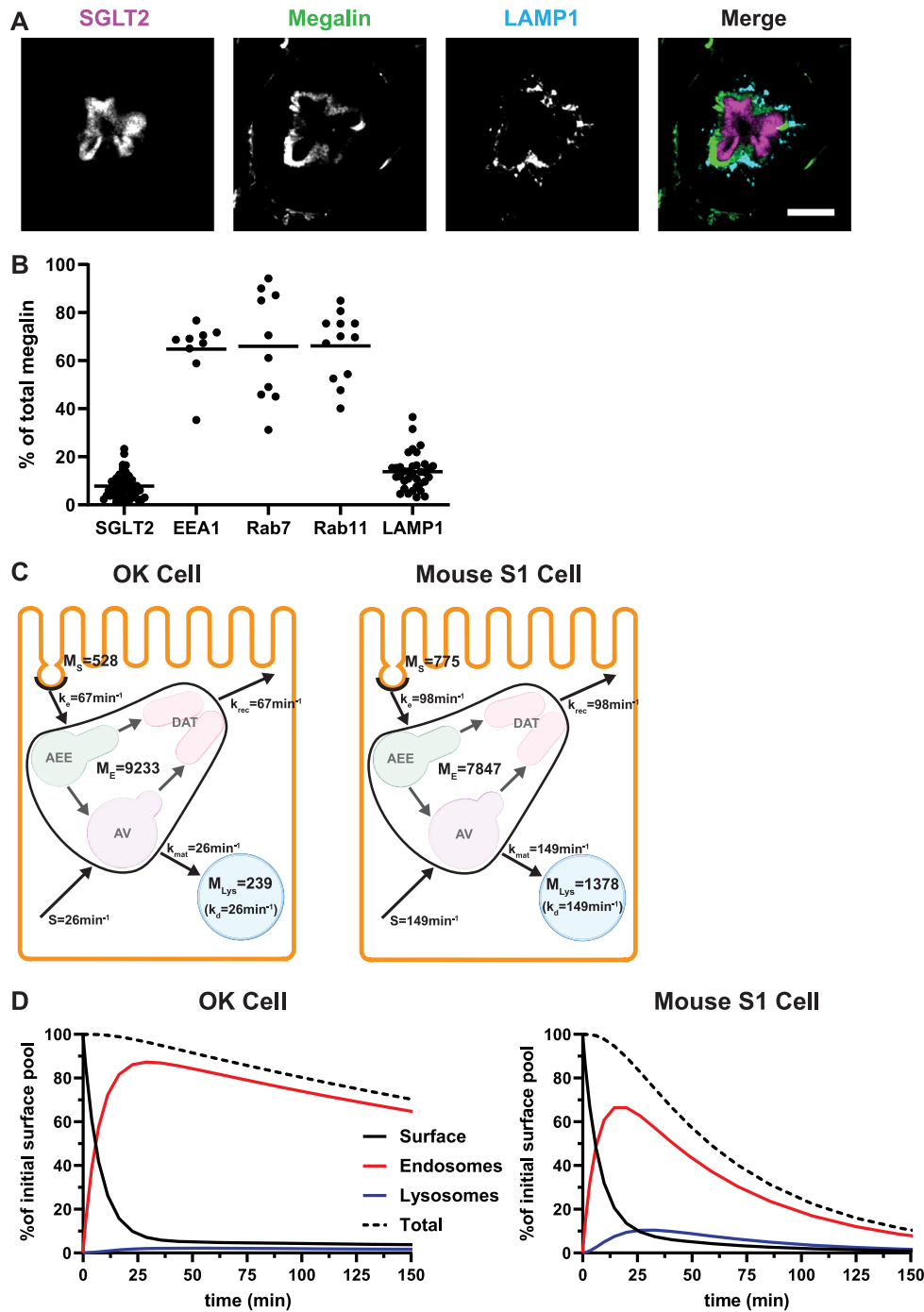
Figure 6. Model of megalin traffic in S1 segment of mouse PT. Cortical kidney sections from 24 wk old female 129/Sv mouse were stained to label SGLT2, megalin, and LAMP1. (A) Representative sum projection images (20 planes) of megalin colocalization with SGLT2 and LAMP1 in an end-on tubule are shown. Scale bar: 10 μm. The weak staining on the basal aspect of the tubule in the megalin channel is due to background binding of the secondary antibody (see Figure S6F). (B) Colocalization of megalin with SGLT2 ($n = 46$, from 5 mice), EEA1 ($n = 9$, from 1 mouse), Rab7 ($n = 10$, from 1 mouse), Rab11a ($n = 12$, from 1 mouse), and LAMP1 ($n = 35$, from 5 mice), quantified by Manders' coefficient over the entire z-stack, is plotted as a % of total megalin. Each point represents a single end-on tubule. (C) A graphical representation of the abridged model of megalin traffic comparing OK cells and S1 segment of mouse PT. Megalin is divided into a surface pool (M_S), an intracellular pool within endosomes (M_E) that comprises AEEs, AVs, and DATs, and a lysosomal pool (M_{Lys}). Values within the pools denote the steady-state distribution of 10,000 molecules of megalin. Kinetic rate values are the number of molecules trafficked through that route per minute. (D) The predicted trajectory of the surface pool of megalin at time 0 min through each pool in the abridged model is simulated, with the synthesis rate set to zero as in Figure 4D. The endosome pool includes AEEs, AVs, and DATs as shown in panel C. The total megalin remaining from the initial surface pool is plotted with black dashed line.

marker Rab4 (~9%). Rab4 was localized very close to the apical membrane, sometimes concentrated at the cell periphery, and colocalized almost entirely with Rab7 and/or Rab11a (93% and 42%, respectively). These data suggest the possibility that Rab4 may have an accessory role in recycling or may mediate the trafficking of a subset of cargoes, such as tight junction proteins. Studies in other epithelial cells and in endothelial cells suggest that Rab4 may be critical for the fast recycling of some tight junction proteins.[46,47] Given the extraordinary capacity of the PT apical endocytic pathway, it is notable that the classical marker of the "fast recycling" pathway does not appear to operate in the recycling of megalin in these cells. Our work here corrects prior assumptions about the relevance of endocytic recycling models based on nonpolarized cells, and highlights the importance of using polarized cells when studying trafficking of megalin and other proteins in the PT.

Our mathematical model provides useful kinetic parameters to describe megalin traffic in the PT. Based on the model, we conclude that AEEs are short lived and rapidly mature into AVs. Determining concrete values for k_{m1}, $k_{DAT,f}$, and $k_{DAT,s}$ necessitated that we provide a value for the fraction of megalin that recycles from AVs versus AEEs, a parameter that cannot readily be determined experimentally. While our model includes "fast" and "slow" recycling pathways in which recycling megalin can enter DATs from both AEEs and AVs, our data demonstrating that more megalin and Rab11a colocalized with Rab7 than with EEA1 suggest that DATs originate preferentially from AVs. We made the starting assumption that a little more than half of recycling megalin (51%) traffics through AVs. Even assuming this low value, megalin "matures" very rapidly from AEEs to AVs. Indeed, because its residence time in DATs is the rate limiting step in recycling, our assumption regarding the fraction of recycling megalin that traffics through AVs has no effect on the overall fractional rate of or amount of megalin molecules recycling, and therefore does not alter the conclusions that we can draw from this model. However, while our data suggest the existence of a single recycling pathway that initiates stochastically from maturing endosomes, it is possible that physiologic or pathologic conditions exist where AEE maturation or recycling from AEEs and AVs are differentially regulated.

Model sensitivity analysis suggests that the rates determining megalin recycling [fast and slow entry to DATS ($k_{DAT,f}$ and $k_{DAT,s}$, respectively) and the return to apical surface from DATs (k_r)] have the largest impact on the fraction of megalin at surface outside of the endocytic rate. Therefore, these rates also have the largest impact on PT endocytic capacity. The rates may be altered in response to stimuli such as changes in flow rate, which occur as a result of changes in glomerular filtration rate. Previously, we and others have demonstrated that OK cells acutely modulate endocytic capacity in response to changes in fluid shear stress.[25,48,49] PT cells may modulate the recycling of megalin to alter the number of receptors available on the surface. For example, phosphorylation of a PPPSP motif on the cytoplasmic tail of megalin has been linked to negative regulation of megalin recycling.[50] Alternatively, membrane flux rates could be regulated by the activation/deactivation of Rab proteins and their effectors.

We demonstrated that differentiated OK cells, which most closely resemble cells of the S1 segment of the PT, recapitulate the organization of the endocytic pathway and the overall distribution of megalin observed in mouse S1 segment cells.[27–30] We confirmed that most megalin (>92%) is intracellular at steady state, and that a large fraction of megalin colocalized with Rab11a. This distribution indicates, as in OK cells, that the recycling rate of megalin is considerably slower than its endocytic rate and likely represents the critical rate determinant of megalin endocytic capacity in the mouse S1 segment. However, our conclusions are limited by the inability to perform biochemical studies in vivo. Additionally, we were unable to quantify the distribution of megalin among the endosomal compartments in vivo with the same resolution as in OK cells, which themselves have a very compact endocytically active region. The very high degree of colocalization between markers of distinct endocytic markers that we observed could be due to a higher density or greater volume of AEEs, AVs, and DATs in the subapical region of the mouse S1 cells and/or to challenges in imaging cells in convoluted tubular geometries. In addition, or alternatively, the considerable overlap between EEA1, Rab7, and Rab11a could reflect even faster maturation of AEEs and entry of megalin into recycling compartments than we measured in OK cells. Assuming comparable fractional rates for endocytosis and degradation of megalin, our model estimates that in vivo intracellular trafficking rates in the S1 segment are on average 2–6 times faster than in our OK cell model. Previous studies have demonstrated that the expression and distribution of megalin, its adaptor protein Dab2, and other endocytic markers vary across the different PT subsegments (S1, S2, and S3).[40,51,52] Thus, it is likely that megalin trafficking kinetics will differ along the length of the PT. Another consideration in the adaptation of our model to the mouse PT is the reliance on data from a limited number of animals. While we consistently found only a small fraction of megalin at the apical surface in a large number of S1 segments, the distribution of megalin between surface and intracellular pools may be sensitive to GFR, and/or acutely modulated by other physiologic cues.

In summary, our data support the utility of OK cells cultured under continuous orbital shear stress as a physiologically relevant model to unravel the regulation of membrane trafficking in S1 segment cells. This model can be readily adapted to understand the impact of genetic mutations and other disease conditions that impair endocytic recovery of filtered ligands and identify the molecular mechanisms impacted. Furthermore, these models of megalin trafficking at the cellular level can be combined with our recent model profiling uptake along the PT-axis to create testable predictions of how filtered ligands are handled during normal variations in physiologic function, or in response to clinically relevant drug treatments, nephrotoxic agents, or other disease conditions.[3,53,54]

Supplementary Material

Supplementary material is available at the *APS Function* online.

Conflict of Interest

The authors have no conflict of interest. O.A.W. holds the position of Editorial Board Member for *Function* and is blinded from reviewing or making decisions for the manuscript.

Data Availability

The data underlying this article are available in the article and in its online supplementary material.

References

1. Christensen EI, Birn H, Storm T, Weyer K, Nielsen R. Endocytic receptors in the renal proximal tubule. *Physiology (Bethesda)*. 2012;**27**(4):223–236.

2. Eshbach ML, Weisz OA. Receptor-Mediated Endocytosis in the Proximal Tubule. *Annu Rev Physiol*. 2017;**79**(1):425–448.

3. Edwards A, Long KR, Baty CJ, Shipman KE, Weisz OA. Modelling normal and nephrotic axial uptake of albumin and other filtered proteins along the proximal tubule. *J Physiol*. 2022;**600**(8):1933–1952.

4. Lazzara MJ, Deen WM. Model of albumin reabsorption in the proximal tubule. *Am J Physiol Renal Physiol*. 2007;**292**(1):F430–F439.

5. Christensen EI, Kristoffersen IB, Grann B, et al. A well-developed endolysosomal system reflects protein reabsorption in segment 1 and 2 of rat proximal tubules. *Kidney Int*. 2021;**99**(4):841–853.

6. Weisz OA. Endocytic adaptation to functional demand by the kidney proximal tubule. *J Physiol*. 2021;**599**(14):3437–3446.

7. Moestrup SK, Verroust PJ. Megalin- and cubilin-mediated endocytosis of protein-bound vitamins, lipids, and hormones in polarized epithelia. *Annu Rev Nutr*. 2001;**21**(1):407–428.

8. Larsen C, Etzerodt A, Madsen M, et al. Structural assembly of the megadalton-sized receptor for intestinal vitamin B12 uptake and kidney protein reabsorption. *Nat Commun*. 2018;**9**(1):5204.

9. Ahuja R, Yammani R, Bauer JA, et al. Interactions of cubilin with megalin and the product of the amnionless gene (AMN): effect on its stability. *Biochem J*. 2008;**410**(2):301–308.

10. Moestrup SK, Kozyraki R, Kristiansen M, et al. The intrinsic factor-vitamin B12 receptor and target of teratogenic antibodies is a megalin-binding peripheral membrane protein with homology to developmental proteins. *J Biol Chem*. 1998;**273**(9):5235–5242.

11. Leheste JR, Rolinski B, Vorum H, et al. Megalin knockout mice as an animal model of low molecular weight proteinuria. *Am J Pathol*. 1999;**155**(4):1361–1370.

12. Nykjaer A, Fyfe JC, Kozyraki R, et al. Cubilin dysfunction causes abnormal metabolism of the steroid hormone 25(OH) vitamin D(3). *Proc Natl Acad Sci*. 2001;**98**(24):13895–13900.

13. Rodman JS, Kerjaschki D, Merisko E, Farquhar MG. Presence of an extensive clathrin coat on the apical plasmalemma of the rat kidney proximal tubule cell. *J Cell Biol*. 1984;**98**(5):1630–1636.

14. Rodman JS, Seidman L, Farquhar MG. The membrane composition of coated pits, microvilli, endosomes, and lysosomes is distinctive in the rat kidney proximal tubule cell. *J Cell Biol*. 1986;**102**(1):77–87.

15. Nielsen S. Endocytosis in proximal tubule cells involves a two-phase membrane-recycling pathway. *Am J Physiol Cell Physiol*. 1993;**264**(4 Pt 1):C823–C835.

16. Hatae T, Fujita M, Sagara H, Okuyama K. Formation of apical tubules from large endocytic vacuoles in kidney proximal tubule cells during absorption of horseradish peroxidase. *Cell Tissue Res*. 1986;**246**(2):271–278.

17. Hatae T, Ichimura T, Ishida T, Sakurai T. Apical tubular network in the rat kidney proximal tubule cells studied by thick-section and scanning electron microscopy. *Cell Tissue Res*. 1997;**288**(2):317–325.

18. Sheff DR, Daro EA, Hull M, Mellman I. The receptor recycling pathway contains two distinct populations of early endosomes with different sorting functions. *J Cell Biol*. 1999;**145**(1):123–139.

19. Birn H, Christensen EI, Nielsen S. Kinetics of endocytosis in renal proximal tubule studied with ruthenium red as membrane marker. *Am J Physiol*. 1993;**264**(2 Pt 2):F239–50.

20. Christensen EI. Rapid membrane recycling in renal proximal tubule cells. *Eur J Cell Biol*. 1982;**29**(1):43–49.

21. Perez Bay AE, Schreiner R, Benedicto I, et al. The fast-recycling receptor Megalin defines the apical recycling pathway of epithelial cells. *Nat Commun*. 2016;**7**(1):11550.

22. Apodaca G, Katz LA, Mostov KE. Receptor-mediated transcytosis of IgA in MDCK cells is via apical recycling endosomes. *J Cell Biol*. 1994;**125**(1):67–86.

23. Leung SM, Ruiz WG, Apodaca G. Sorting of membrane and fluid at the apical pole of polarized Madin–Darby canine kidney cells. *Mol Biol Cell*. 2000;**11**(6):2131–2150.

24. Mattila PE, Raghavan V, Rbaibi Y, Baty CJ, Weisz OA. Rab11a-positive compartments in proximal tubule cells sort fluid-phase and membrane cargo. *Am J Physiol Cell Physiol*. 2014;**306**(5):C441–C449.

25. Long KR, Shipman KE, Rbaibi Y, et al. Proximal tubule apical endocytosis is modulated by fluid shear stress via an mTOR-dependent pathway. *Mol Biol Cell*. 2017;**28**(19):2508–2517.

26. Ren Q, Gliozzi ML, Rittenhouse NL, et al. Shear stress and oxygen availability drive differential changes in opossum kidney proximal tubule cell metabolism and endocytosis. *Traffic*. 2019;**20**(6):448–459.

27. Park HJ, Fan Z, Bai Y, et al. Transcriptional programs driving shear stress-induced differentiation of kidney proximal tubule cells in culture. *Front Physiol*. 2020;**11**:587358.

28. Eshbach ML, Sethi R, Avula R, et al. The transcriptome of the Didelphis virginiana opossum kidney OK proximal tubule cell line. *Am J Physiol Renal Physiol*. 2017;**313**(3):F585–F595.

29. Lee JW, Chou C-L, Knepper MA. Deep sequencing in microdissected renal tubules identifies nephron segment-specific transcriptomes. *J Am Soc Nephrol*. 2015;**26**(11):2669–2677.

30. Chen L, Chou C-L, Knepper MA. A Comprehensive Map of mRNAs and their isoforms across all 14 renal tubule segments of mouse. *J Am Soc Nephrol*. 2021;**32**(4):897–912.

31. Long KR, Rbaibi Y, Bondi CD, et al. Cubilin-, megalin-, and Dab2-dependent transcription revealed by CRISPR/Cas9 knockout in kidney proximal tubule cells. *Am J Physiol Renal Physiol*. 2022;**322**(1):F14–F26.

32. Khundmiri SJ, Chen L, Lederer ED, Yang C-R, Knepper MA. Transcriptomes of major proximal tubule cell culture models. *J Am Soc Nephrol*. 2021;**32**(1):86–97.

33. Zou Z, Chung B, Nguyen T, et al. Linking receptor-mediated endocytosis and cell signaling: evidence for regulated

intramembrane proteolysis of megalin in proximal tubule. *J Biol Chem*. 2004;**279**(33):34302–34310.

34. Negoescu A, Labat-Moleur F, Lorimier P, et al. F(ab) secondary antibodies: a general method for double immunolabeling with primary antisera from the same species. Efficiency control by chemiluminescence. *J Histochem Cytochem*. 1994;**42**(3):433–437.

35. Bolte S, Cordelières FP. A guided tour into subcellular colocalization analysis in light microscopy. *J Microsc*. 2006;**224**(Pt 3):213–232.

36. Schneider CA, Rasband WS, Eliceiri KW. NIH Image to ImageJ: 25 years of image analysis. *Nat Methods*. 2012;**9**(7):671–675.

37. Manders EMM, Verbeek FJ, Aten JA. Measurement of colocalization of objects in dual-colour confocal images. *J Microsc*. 1993;**169**(3):375–382.

38. Cresawn KO, Potter BA, Oztan A, et al. Differential involvement of endocytic compartments in the biosynthetic traffic of apical proteins. *EMBO J*. 2007;**26**(16):3737–3748.

39. Grieco G, Janssens V, Gaide Chevronnay HP, et al. Vps34/PI3KC3 deletion in kidney proximal tubules impairs apical trafficking and blocks autophagic flux, causing a Fanconi-like syndrome and renal insufficiency. *Sci Rep*. 2018;**8**(1):14133.

40. Christensen EI, Nielsen S, Moestrup SK, et al. Segmental distribution of the endocytosis receptor gp330 in renal proximal tubules. *Eur J Cell Biol*. 1995;**66**(4): 349–364.

41. Borchers A-C, Langemeyer L, Ungermann C. Who's in control? Principles of Rab GTPase activation in endolysosomal membrane trafficking and beyond. *J Cell Biol*. 2021;**220**(9): e202105120.

42. Grant BD, Donaldson JG. Pathways and mechanisms of endocytic recycling. *Nat Rev Mol Cell Biol*. 2009;**10**(9): 597–608.

43. Stenmark H. Rab GTPases as coordinators of vesicle traffic. *Nat Rev Mol Cell Biol*. 2009;**10**(8):513–525.

44. Ren Q, Weyer K, Rbaibi Y, et al. Distinct functions of megalin and cubilin receptors in recovery of normal and nephrotic levels of filtered albumin. *Am J Physiol Renal Physiol*. 2020;**318**(5):F1284–F1294.

45. Vallon V, Platt KA, Cunard R, et al. SGLT2 mediates glucose reabsorption in the early proximal tubule. *J Am Soc Nephrol*. 2011;**22**(1):104–112.

46. Stamatovic SM, Sladojevic N, Keep RF, Andjelkovic AV. Relocalization of junctional adhesion molecule A during inflammatory stimulation of brain endothelial cells. *Mol Cell Biol*. 2012;**32**(17):3414–3427.

47. Bruewer M, Utech M, Ivanov AI, et al. Interferon-gamma induces internalization of epithelial tight junction proteins via a macropinocytosis-like process. *FASEB J*. 2005;**19**(8):923–933.

48. Raghavan V, Rbaibi Y, Pastor-Soler NM, Carattino MD, Weisz OA. Shear stress-dependent regulation of apical endocytosis in renal proximal tubule cells mediated by primary cilia. *Proc Natl Acad Sci*. 2014;**111**(23):8506–8511.

49. Ferrell N, Ricci KB, Groszek J, Marmerstein JT, Fissell WH. Albumin handling by renal tubular epithelial cells in a microfluidic bioreactor. *Biotechnol Bioeng*. 2012;**109**(3):797–803.

50. Yuseff MI, Farfan P, Bu G, Marzolo M-P. A cytoplasmic PPPSP motif determines megalin's phosphorylation and regulates receptor's recycling and surface expression. *Traffic*. 2007;**8**(9):1215–1230.

51. Limbutara K, Chou C-L, Knepper MA. Quantitative proteomics of all 14 renal tubule segments in rat. *J Am Soc Nephrol*. 2020;**31**(6):1255–1266.

52. Schuh CD, Polesel M, Platonova E, et al. Combined structural and functional imaging of the kidney reveals major axial differences in proximal tubule endocytosis. *J Am Soc Nephrol*. 2018;**29**(11):2696–2712.

53. Edwards A, Christensen EI, Unwin RJ, Norden AGW. Predicting the protein composition of human urine in normal and pathological states: quantitative description based on Dent1 disease (CLCN5 mutation). *J Physiol*. 2021;**599**(1):323–341.

54. Gliozzi ML, Espiritu EB, Shipman KE, et al. Effects of proximal tubule shortening on protein excretion in a lowe syndrome model. *J Am Soc Nephrol*. 2020;**31**(1):67–83.